Using sea surface temperature observations to constrain upper ocean properties in an Arctic sea ice-ocean data assimilation system

Xi Liang[1*], Martin Losch[2], Lars Nerger[2], Longjiang Mu[2],
Qinghua Yang[3,4,5], Chengyan Liu[6,7]

[1]Key Laboratory of Research on Marine Hazards Forecasting, National Marine Environmental Forecasting Center, Beijing, China

[2]Alfred-Wegener-Institut, Helmholtz Zentrum für Polar- und Meeresforschung, Bremerhaven, Germany

[3]Guangdong Province Key Laboratory for Climate Change and Natural Disaster Studies, School of Atmospheric Sciences, Sun Yat-sen University, Zhuhai, China

[4]State Key Laboratory of Numerical Modeling for Atmospheric Sciences and Geophysical Fluid Dynamics, Institute of Atmospheric Physics, Chinese Academy of Sciences, Beijing, China

[5]Southern Laboratory of Ocean Science and Engineering (Guangdong, Zhuhai), Zhuhai, China

[6]International Polar Environment Research Laboratory, College of Oceanography, Hohai University, Nanjing, China

[7]Schoolof Marine Sciences, Nanjing University of Information Science and Technology, Nanjing, China

Corresponding author: Xi Liang, Key Laboratory of Research on Marine Hazards Forecasting, National Marine Environmental Forecasting Center, 8 Dahuisi Road, Beijing 100081, China. (liangx@nmefc.cn)

Key points:

- *Sea surface temperature assimilation improves upper ocean temperature, sea ice edge and marginal sea ice thickness simulations.*
- *Simulated upper ocean temperatures improve more where vertical convection processes are more important.*
- *Sea ice edge and thickness simulations are improved due to the correction of the SST bias.*

Abstract

Sea ice data assimilation can greatly improve forecasts of Arctic sea ice evolution. Many previous sea ice data assimilation studies were conducted without assimilating ocean state variables, even though the sea ice evolution is closely linked to the oceanic conditions, both dynamically and thermodynamically. Based on the method of a localized ensemble error subspace transform Kalman filter, satellite-retrieved sea ice concentration and sea ice thickness are assimilated into an Arctic sea ice-ocean model. As a new addition, sea surface temperature (SST) data is also assimilated. The additional assimilation of SST improves not only the simulated ocean temperature in the mixed layer of the ocean substantially but also the accuracy of sea ice edge position, sea ice extent, and sea ice thickness in the marginal sea ice zone. The improvement in the simulated potential temperature in the upper 1000 m can be attributed to the enhanced vertical convection processes in the regions where the assimilated observational SST is colder than the simulated SST without assimilation. The improvements in the sea ice edge position and sea ice thickness simulations are primarily caused by the SST data assimilation reducing biases in the simulated SST and the associated coupled ocean-sea ice processes. Our investigation suggests that, due to the complex interaction between the sea ice and ocean, assimilating ocean data should be an indispensable component of numerical polar sea-ice forecasting systems.

Key words: sea ice concentration, sea ice thickness, SST, data assimilation, upper ocean temperature, sea ice edge

1. Introduction

Arctic sea ice has been decreasing significantly over the past three decades (Comiso et al., 2008; Gao et al., 2015). This change is accompanied by more frequent navigation activities in the Arctic Ocean (Rojas-Romagosa et al., 2016). The route distance saved between Northwestern Europe and Northeastern Asia through the Arctic Ocean can be as high as 50% compared to the traditional low-latitude shipping lanes. Along with economic benefits, potential risks still threaten marine safety in the Arctic Ocean all the time, such as thick floating ice, storms, and heavy fog. Arctic environmental forecasts have played an important role in guaranteeing the marine safety (Jung et al., 2016). Operational sea ice forecasts are carried out by many departments all over the world, for example, the U.S Navy Arctic Cap Nowcast/Forecast System (ACNFS; Posey et al., 2010) provides 7 days forecasts of sea ice concentration, sea ice thickness, sea ice drift, ocean temperature, ocean salinity and ocean current forecasts in northern hemisphere (poleward of 40 °N). The Canadian Global Ice Ocean Prediction System (GIOPS; Smith et al., 2016) provides global 10 days forecasts of ocean and sea ice states covering the Arctic Ocean including sea ice concentration, sea ice thickness and sea ice drift. The Mercator PSY4Q system (Lellouche et al., 2013) provides global 9 days forecasts of sea ice concentration, sea ice thickness, sea ice velocity, ocean temperature, ocean salinity and ocean current. The Danish Meteorological Institute HYCOM-CICE system (Madsen et al., 2015) provides 6 days forecasts of sea ice and ocean states covering the Atlantic Ocean north of 20 °S and the Arctic Ocean.

In numerical synoptic-scale forecasting models, data assimilation is a critical component to reduce the uncertainties associated with initial fields and systematic model errors. Sea ice and ocean data assimilation schemes are widely used in state-of-the-art operational Arctic forecasting systems (Sakov et al., 2012; Posey et al., 2010). Observational data can be assimilated in a variety of methods. For example, the U.S Navy ACNFS uses a 3-Dimensional VARiational (3D-VAR) scheme to assimilate both sea ice and ocean observations. The Norwegian TOPAZ4 system (Sakov et al., 2012) uses an Ensemble Kalman Filter (EnKF; Evensen, 1994; Anderson, 2001) to assimilate sea ice concentration, sea ice drift, sea level anomaly, SST, as well as in situ profile observations of temperature and salinity. The Canadian GIOPS uses a combination of a 3D-VAR scheme to assimilate sea ice observations and a reduced order Kalman filter to assimilate ocean observations. In this study, we employ the ensemble Error Subspace Transform Kalman Filter (ESTKF; Nerger et al., 2012a), and focus on the effects of additional ocean data assimilation on a sea-ice prediction system.

The location of the sea ice edge is extremely important for marine safety (Goessling et al., 2016). In the Arctic Ocean, due to the presence of a sea ice edge, the sea ice-ocean system is characterized by strong anisotropies and non-stationary features (Lisæter et al., 2003). Sakov et al. (2012) demonstrated that the correlation between sea ice concentration and sea surface salinity at the ice edge, is strongly anisotropic and changes dynamically. Because of the rapidly changing system, data assimilation schemes with stationary background covariances, such as 3D-VAR and optimal interpolation, may not be flexible enough to accurately capture the dynamics of the coupled sea ice-ocean system. In our study, we chose a data assimilation scheme from the family of EnKFs, which has the advantage of a non-stationary state error covariance, that we find suitable for assimilating sea ice and ocean data. Data assimilation almost trivially improves the forecasts of fields for which observations are assimilated. Furthermore, systems based on EnKF data assimilation schemes can be multivariate and can hence enhance also the forecast of unobserved variables if clear statistical correlations exist between them and the observed variables that reflect their physical relationship. For example, the assimilation of sea ice concentration improved sea ice thickness forecasts in the melting and freezing seasons due to the positive correlation between the sea ice concentration and the sea ice thickness (Yang et al., 2015a, 2015b; Yang et al., 2016). The assimilation of sea ice thickness improved the forecasts of the sea ice concentration and ocean surface characteristics (Lisæter et al., 2007; Yang et al., 2014; Fritzner et al., 2019; Zhang et al., 2018). Assimilating sea surface temperature also improved the sea ice thickness forecasts during the melting season (Liang et al., 2017).

Mu et al. (2018b) introduced an ensemble ESTKF data assimilation scheme into the Massachusetts Institute of Technology general circulation model (MITgcm; Marshall et al., 1997) and assimilated sea ice concentration and thickness observations. They found that the sea ice thickness simulation substantially improved by the thickness assimilation, whereas the improvement in the simulated sea ice concentration was small. To further address this issue, we will simultaneously assimilate satellite-retrieved sea ice concentration, sea ice thickness, and SST observations into the MITgcm based on the ensemble ESTKF scheme with localized analysis. The remainder of this paper is organized as follows. Section 2 describes the model configuration, data assimilation scheme, data sets and the experiment design. Section 3 assesses the Arctic ocean and sea ice simulations with and without SST assimilation. Discussion and conclusion are given in section 4.

2. Methods

2.1 Coupled Regional Sea Ice-Ocean Model

Our Arctic configuration of the MITgcm has an average horizontal resolution of 18 km and covers the whole Arctic Ocean with open boundaries close to 55 °N in both the Atlantic and Pacific sectors (Losch et al., 2010). The ocean model includes 420×384 horizontal grid points, 50 vertical model layers with 28 vertical layers in the top 1000 m. The thickness of the ocean vertical layers increases from 10 m near the surface to 456 m near the bottom.

The sea ice model within the MITgcm uses a viscous-plastic rheology and zero-layer thermodynamics with two thickness categories: open water and sea ice (Losch et al., 2010). The sea ice momentum equations are solved following Zhang and Hibler (1997). The sea ice model shares the same horizontal grid with the ocean model.

The open boundary conditions are derived from a historical run of a global cubed-sphere configuration of the MITgcm (Menemenlis et al., 2008). The atmospheric forcing data are the 23 ensemble forecasts of the United Kingdom Met Office Unified Model (UKMO UM; Bowler et al., 2008; obtained from http://tigge.ecmwf.int/). Further details about the model configuration can be found in Mu et al. (2018b).

2.2 Data assimilation scheme

The data assimilation scheme used in this study is an ensemble-based Error Subspace Transform Kalman Filter (ESTKF; Nerger et al., 2012a) with localization. The ESTKF combines the high accuracy and efficiency of the Singular Evolutive Interpolated Kalman filter (SEIK; Pham, 2001) that has been used with the MITgcm by, for example, Mu et al. (2018a), with ensemble transformation of the Ensemble Transform Kalman Filter (ETKF; Bishop et al., 2001). The ESTKF provides consistent projections between the ensemble space and the error subspace with a minimal ensemble transformation of the ensemble members. To increase the impact of the ESTKF and to avoid that the ensemble spread is reduced too much by the analysis step, a horizontal localization scheme is applied in the ESTKF following Nerger et al. (2006). The localized filter changes the model fields at each model grid column separately using only observations within a specified influence radius (denoted localization radius) around this location. Further each observation is weighted to decrease the influence of each available observation with increasing distance between the analysis and observation locations. For a complete description of the algorithm see, e.g. Androsov et al. (2019).

In this study, the localized ESTKF scheme is used as implemented in the Parallel Data Assimilation Framework (PDAF; Nerger and Hiller, 2013). A complete ensemble data assimilation cycle starts from an initial ensemble and normally includes three alternating steps: forecast, analysis, and adjustment. The ensemble includes many model state realizations that together represent the state estimate and its uncertainty. In the forecast step, all ensemble states, as a set of parallel runs, are driven by external forcing from a set of new restart files to the next time when new observations become available. In the analysis step, the model fields of each ensemble state are arranged into a model state vector. The model state vectors of all runs constitute an ensemble matrix. Then a loop over all surface grid points is performed for the local analysis. For each surface grid point to be updated, observations within the influence radius around the updating grid point are collected into an observation vector and a localization weighting algorithm is applied to the observation error covariance matrix. The data assimilation algorithm uses the ensemble matrix, observation vector and observation error covariance matrix. The analysis transforms the ensemble matrix holding the forecast state vectors into a matrix of analysis state vectors by incorporating the observational information into the model states. Note that most data assimilation schemes are purely mathematical methods without physical constraints. In the adjustment step, a post-assimilation algorithm is carried out that examines and modifies the analysis state vectors according to physical constraints and relationships among variables. Finally, a new set of ensemble states is initialized with the states from the physically constrained analysis matrix, and a new forecast step is started.

2.3 Data sets

The sea ice concentration and thickness data for the assimilation are the same and processed in the same way as in Mu et al. (2018b). Daily sea ice concentration observations are derived from the Special Sensor Microwave Imager Sounder (SSMIS) sea ice concentration data (Cavalieri and Parkinson 2012; Cavalieri et al., 2012; Kaleschke et al., 2001), which are provided by the University of Hamburg (obtained from http://icdc.cen.uni-hamburg.de/1/daten/cryosphere/seaiceconcentration-asi-ssmi.html). Daily sea ice thickness observations in thin ice area (< 1 m) are derived from the Soil Moisture Ocean Salinity (SMOS) sea ice thickness data (Tian-Kunze et al., 2014). The SMOS sea ice thickness data are retrieved from satellite brightness temperature combined with a sea ice thermodynamic model and a three-layer radiative transfer model (Kaleschke et al., 2010, 2012; obtained from http://icdc.cen.uni-hamburg.de/1/daten/cryosphere/l3c-smos-sit.html). The weekly sea ice thickness observations are derived from the European Space Agency satellite mission CryoSat-2 sea ice thickness data (Wingham et al., 2006; Laxon et al., 2013;

Ricker et al., 2014; obtained from http://data.meereisportal.de/data/cryosat2/version2.0/). The CryoSat-2 sea ice thickness data are retrieved from radar altimetry measurements of sea ice freeboard. The estimated sea ice thickness uncertainties are included in the SMOS and CryoSat-2 data. Both the SMOS and CryoSat-2 sea ice thickness data are only available in winter time from November to April. The SSMIS sea ice concentration, the SMOS and CryoSat-2 sea ice thickness, as well as sea ice thickness uncertainties, are interpolated onto the MITgcm model grid. As the satellite data products are already gridded, we interpolate them onto model grid for convenience. We can assume the interpolation error is not larger than that for interpolating the model variable onto the data grid.

Daily SST observations for assimilation are derived from the GHRSST Multi-Product Ensemble (GMPE) data, which are provided by the UKMO. The GMPE SST data is a near-real-time Level-4 satellite-retrieved product with a horizontal resolution of 0.25 degrees (obtained from http://marine.copernicus.eu/, product identifier: SST_GLO_SST_L4_NRT_OBSERVATIONS_010_005). Within the framework of the Group for High Resolution Sea Surface Temperature (GHRSST) project, the GMPE system produces daily global SST maps that computed as the median of a large number of SST products by various institutes around the world. Each product contributing to the GMPE product uses different observational data sets including both in situ and satellite SST data that are then combined with a model as a reanalysis product. Derived from multi-product ensemble data, the GMPE SST data product greatly reduces measurement uncertainties. The GMPE SST data cover the ice free area in the Arctic Ocean. Figure 1 shows days with available temperature observations and mean uncertainties of the observations in 2012 in the GMPE SST data. The SST observations are available for more than 300 days in the high latitude North Atlantic Ocean, the Labrador Sea, the Greenland Sea, the Norwegian Sea, the Barents Sea and the Bering Sea. The SST observations are available for 90 days to 210 days in most of the Arctic marginal seas, and for less than 60 days in the central Arctic Ocean. The mean uncertainties are lower than 0.4 °C in most of the areas where observations are available for more than 300 days. In most of the Arctic marginal seas the mean uncertainties are higher than 1 °C. Large uncertainties exist in the coastal areas of the Beaufort Sea, the Kara Sea and the Laptev Sea. The GMPE SST data, as well as its uncertainties, are interpolated onto the MITgcm model grid.

Here we use four kinds of in situ ocean observations in 2012 to validate the simulated potential temperature in ice free regions. (1) Argo standard depth level (Argo SDL) data are produced by International Pacific Research Center by interpolating global Argo temperature and salinity profiles onto 26 standard levels between 0 and 2000 m depths. They are available since October 2010 (obtained from http://apdrc.soest.hawaii.edu/projects/Argo/data/profiles/). (2) Glider data are collected by Autonomous Profiling Explorer (APEX) profiling float system and processed by French Research Institute for Exploitation of the Sea (IFREMER). They provide vertical temperature profiles in the high latitude North Atlantic Ocean. Most of the profiles reach 1000 m deep. (3) Shipboard Conductivity-Temperature-Depth (CTD) data, managed by the Norwegian Marine Data Center, provide vertical temperature profiles along the coast of Norway and Svalbard Island. Most of the profiles are hundreds of meters deep. (4) Along-trajectory data, collected by IFREMER, provide sea surface temperature records along the fixed seaway between Denmark and Greenland (The Glider, CTD, and along-trajectory data were obtained from http://marine.copernicus.eu/, product identifier: INSITU_ARC_TS_REP_OBSERVATIONS_013_037).

Furthermore, additional data sets are used to evaluate the influence of the assimilation of SST data on the sea ice simulation in 2012: (1) sea ice edge observations in March and September derived from sea ice concentration data of the Advanced Microwave Scanning Radiometer (AMSR; Spreen et al., 2008; obtained from http://data.meereisportal.de/data/median_edge/) are used to compare with the simulated sea ice edge, defined as a marginal zone with 15% sea ice concentration. (2) Sea ice extent observations derived from the Multisensor Analyzed Sea Ice Extent-Northern Hemisphere (MASIE-NH; National Ice Center and National Snow and Ice Data Center, 2010; obtained from http://nsidc.org/data/masie/) data are used to compare with the simulated sea ice extent. The MASIE-NH data is provided daily by the National Ice Center Interactive Multisensor Snow and Ice Mapping System with a spatial resolution of 4 km. (3) Moored upward-looking sonar (ULS) ice draft observations from the Beaufort Gyre Exploration Project (BGEP; Proshutinsky et al., 2005; obtained from http://www.whoi.edu/beaufortgyre) are available at three positions in the Beaufort Gyre. They are used to compare with the simulated sea ice thickness. The ULS samples the ice draft with a precision of 0.1 m (Melling et al., 1995), and the ice draft can be converted to ice thickness by multiplying a factor of

1.1 (Nguyen et al., 2011).

2.4 Experiment design

To assess the effects of the SST assimilation on the simulated sea ice concentration and sea ice thickness, we run three experiments named CTRL, NoSSTasim and SSTasim. The experiment schematic is shown in Figure 2. In all cases the model ensemble includes 23 parallel runs. The CTRL run, aiming to build the reference and its variability which is used to generate the ensemble perturbations, is a purely prognostic experiment without any data assimilation. It is obtained by integrating the model from a historical restart file on 1 Oct 2011 until 31 Dec 2012 driven by the mean UKMO ensemble forcing. Daily snapshots of the model states (sea ice concentration, sea ice thickness, upper 1000 m ocean temperature) during 2012 are stored. After subtracting the mean value from the model states, a singular value decomposition (SVD) is computed from which the 22 leading singular values of the model states' variability are used to generate the ensemble by second-order exact sampling (Pham, 2001).

The NoSSTasim run assimilates the SSMIS sea ice concentration, the SMOS and CryoSat-2 sea ice thickness data as in Mu et al. (2018b). In this run the model state vector for the assimilation includes only include sea ice concentration and sea ice thickness. The observations are assimilated daily followed by an ensemble integration over 24 hours in which each run is forced by one of the 23 ensemble forecasts of the UKMO UM. Forecast error uncertainties of the ensemble can be represented by the UKMO UM 23 atmospheric forecasts, so that there is no need for additional ensemble inflation (Yang et al., 2015a).

The SSTasim run assimilates the same sea ice data as in the NoSSTasim run and additionally the GMPE SST data. The assimilation cycle of the SSTasim run is analogous to that of the NoSSTasim run. Note that here the model state vector includes sea ice concentration, sea ice thickness and upper 1000 m ocean temperature. The observation vector includes sea ice concentration, sea ice thickness and SST. Within the mixed layer, the temperature is strongly correlated to the surface temperature, which can vary on short time scales. In contrast the temperature below the mixed layer develops more slowly. For this physical reason we decide to update the entire mixed layer along with the temperature of the surface level of the model is updated. The temperature at model layers below the mixed layer is not updated by the data assimilation for the reason that the different timescale and the non-Gaussian intermittency of deep convection cannot be properly represented by a prior error covariance. This corresponds to a vertical localization with a step function and a radius equal to the thickness of the mixed layer. The thickness of the mixed layer in the model varies in time and space, so that in some places only surface values are updated and in others almost the entire water column. The mixed layer depth is read from model outputs.

The NoSSTasim and SSTasim runs run from 1 Jan 2012 to 31 Dec 2012. Storing daily snapshots allows us to evaluate the assimilation performance in both wintertime and summertime. The localization radius is set to 12 grid points, corresponding to approximately 216 km. The uncertainties of the SSMIS sea ice concentration data accounting for measurement and representation errors are assumed to be uniform with 25% following Mu et al. (2018b). The post-assimilation process focuses on basic physical relationships among sea ice concentration, sea ice thickness and ocean temperature. Thus, sea ice thickness is set to 0 whenever the sea ice concentration is 0. Further, in the marginal sea ice zone, the sea ice concentration and thickness are set to 0 whenever the surface ocean temperature is warmer than the surface freezing point, because the sea ice can only exist in the simulation where the SST is below surface freezing point. Besides these relationships, we further introduce an ocean surface salinity adjustment parameterization. During the analysis step, sea ice volume change can be generated or destroyed by the data assimilation algorithm. To conserve the net mass, this change in ice volume or thickness requires a corresponding volume change of the surface layer of opposite sign and since sea ice has no salinity in our experiments, conservation of salt in the surface layer implies that the amount of salt in the top layer H_{ocean}, which is 10m in our experiments is the same before and after the analysis step:

$$S_{post}(\rho_{ocean}H_{ocean} - \rho_{ice}\Delta H_{ice}) = S_{pre}\rho_{ocean}H_{ocean}$$

$$\Leftrightarrow S_{post} = \frac{S_{pre}\rho_{ocean}H_{ocean}}{\rho_{ocean}H_{ocean} - \rho_{ice}\Delta H_{ice}}$$

where S_{post} and S_{pre} represent ocean top-layer salinity after and before data assimilation, ρ_{ocean} and ρ_{ice} represent ocean top-layer density and sea ice density, and ΔH_{ice} is sea ice thickness increment due to data assimilation. We use ρ_{ice}= 880 kg*m^{-3}

and ρ_{ocean}=1027 kg*m^{-3}. Note that this procedure needs to be adjusted if sea ice is allowed to be saline.

3. Results

3.1 Overall assimilation effect

The model state differences between simulations with and without data assimilation illustrate the data assimilation effects. Figure 3 shows the spatial distributions of root mean square difference (RMSD) between the experiments NoSSTasim and CTRL (left column) and between SSTasim and NoSSTasim (right column) for the model state variables sea ice concentration, sea ice thickness, and SST. The RMSDs are derived from calculating corresponding model states on daily basis in 2012 and show how strongly the assimilation changes the fields.

Similar to the impact of sea ice assimilation on the sea ice variables, the impact of the SST assimilation on the simulated SST is as expected (Figure 3b). The RMSDs between the model states with and without data assimilation correspond to the deviations between the assimilated observations and the model states without data assimilation, which are reduced by the data assimilation. The SST assimilation affects the SST in ice free regions with large differences around Svalbard, along the southern coast of Greenland, in the areas east of Iceland, in the Labrador Sea and Beaufort Seas (Figure 3b). This corresponds to the annual mean SST biases between the NoSSTasim run and the GMPE SST data which reach an amplitude of up to 4 °C in these regions (Figure 4). The sea ice assimilation affects the sea ice concentrations with large changes in the marginal sea ice zone both in the Atlantic and Pacific sectors (Figure 3c), where the CTRL run is biased with a broader marginal sea ice zone than the SSMIS data (we discuss these biases in section 3.4). Large changes in the sea ice thickness exist in the regions of multiyear ice in the Arctic Ocean and along the eastern coast of Greenland where sea ice is exported from the Arctic (Figure 3e). In these areas, the simulated sea ice thickness in the CTRL run is overall thicker than that in the CryoSat-2 data (not shown).

We note for the discussion in section 4 that the physical processes implemented in the sea ice-ocean model induce indirect effects of the assimilation: The SST assimilation affects the sea ice state and, vice versa, sea ice assimilation affects the SST. The assimilation of sea ice data has the largest effect on the SST in the marginal sea ice zones, such as the Greenland Sea and the Bering Sea (Figure 3a). The SST assimilation has strong effects on the sea ice concentration in the thin ice regions, such as the Greenland Sea, the Barents Sea, the Kara Sea and the Chukchi Sea (Figure 3d). Sea ice thickness is affected notably by the SST assimilation along the eastern coast of Greenland (Figure 3f).

Because the GMPE SST data is only available in ice free areas and a localized data assimilation scheme is used, we use the regional mean temperature south of 75 °N to assess the temperature change (Figure 5a). Compared to the NoSSTasim run, the additional GMPE SST data assimilation cools the entire upper ocean down to 1800 m depth. The maximum temperature reduction is close to -1 °C and occurs at 220 m depth. The mean ocean salinity north of 75 °N as a function of depth is shown in Figure 5b. Assimilating sea ice data reduces the ocean surface salinity in the NoSSTasim run. Assimilating GMPE SST data further reduces the ocean surface salinity. The salinity change of the ocean surface layer penetrates to 80 m depth due to the model dynamics.

3.2 Comparison with the Argo SDL data

Most of the Argo profiles in Arctic and sub-Arctic regions are concentrated in the high latitude North Atlantic Ocean, the Labrador Sea, the Greenland Sea, the Norwegian Sea and the Bering Sea. The Argo SDL data set is available on the 26 standard depth levels, specifically 1 level at 5 m, 3 levels from 10 m to 30 m, 5 levels from 50 m to 150 m, 3 levels from 200 m to 300 m, 12 levels from 400 m to 1500 m, and 2 levels from 1750 m to 2000 m, each with equal depth intervals of 10 m, 25 m, 50 m, 100 m and 250 m, respectively. Here, we choose not to explore the seasonal differences of the SST assimilation influence, so we calculate the root mean square error (RMSE) of ocean temperature of the analysis ensemble mean relative to the Argo SDL observations over the full year taking into account all available observations within the model grid in 2012.

Because in the CTRL run we only stored ocean temperature in the upper 1000 m, the CTRL run is evaluated only in the upper 18 standard depth levels (Figure 6a and 6b). Figure 6c shows the number of Argo SDL data values for each standard depth. There are more than 5500 Argo SDL data values at each of the upper 18 levels. Below this the number decreases slowly to 3671 at 2000 m depth. The CTRL run simulates a warmer North Atlantic Ocean and Nordic Sea with the maximum mean bias exceeding 1 °C at 30 m depth (Figure 6b). The RMSE of ocean temperature of the

CTRL run increases from 1.73 °C at 5 m depth to 2.22 °C at 75 m depth, and decreases to 1.2 °C at 900 m depth (Figure 6a). The ocean temperature RMSE of the NoSSTasim run are slightly smaller by 0.05 °C in the upper 500 m. We attribute this improvement to the ocean's response to the more accurate sea ice distribution and ice edge position after assimilating sea ice parameters. The SST assimilation greatly improves the ocean temperature simulation from surface to 1750 m depth. Compared with the NoSSTasim run, the RMSE of ocean temperature of the SSTasim run has been reduced by 0.41 °C in upper 30 m, by 0.35 °C between 50 m and 250 m, by 0.2 °C between 300 m and 400 m, and by 0.1 °C between 1000 m and 1500 m. The warm bias of the NoSSTasim run in the North Atlantic Ocean and the Nordic Sea has been corrected in the upper 1750m with maximal improvements of 0.7 °C in the upper 300 m.

The spatial distributions of the ocean temperature RMSE with respect to the Argo SDL data at 200 m depth are shown in Figure 7. The RMSE of the NoSSTasim run is large in the high latitude central Atlantic Ocean, the southern Norwegian Sea and the Bering Sea. In the SSTasim run, large improvements of ocean temperature simulation are found in the high latitude central Atlantic Ocean and the southern Norwegian Sea. To further describe the ocean temperature RMSE in different areas, the regional mean RMSE at 10 m, 200 m, and 1500m depth are listed in Table 1. In general, the RMSE of the NoSSTasim run with respect to the Argo SDL data is reduced by the additional assimilation of the GMPE SST data in the SSTasim run. The largest reductions are found where the RMSE is also very large, e.g. in the high latitude western Atlantic Ocean at 10m depth, or the high latitude central Atlantic Ocean at 200m depth. The only exception is the deep Bering Sea, where the RMSE is already quite small without SST assimilation and the RMSE in the SSTasim run is larger by 0.09 °C than that in the NoSSTasim run.

3.3 Comparison with the Glider data

All of the Glider profiles used in this study are located in the high latitude North Atlantic Ocean, the Labrador Sea, the Norwegian Sea and the Greenland Sea. Temperature profile observations were collected during ascending phase of the Gliders to enhance the accuracy of the geographic information received by satellites at the end of the ascent. Only profiles flagged as "good data" are used here for the model-data comparison. There are 1988 Glider profiles of which 1902 profiles reach below 800 m. 1507 modeled temperature profiles out of the 1988 profiles, that is approximately 75.8% of the profiles, are improved in the SSTasim run (Figure 8a). For the improved profiles, the mean RMSE with respect to the Glider observations decreases from 1.41 °C of the NoSSTasim run to 0.98 °C of the SSTasim run. For the remaining 24.2% of the profiles (Figure 8b), the mean RMSE with respect to the Glider observations increases from 1.02 °C of the NoSSTasim run to 1.45 °C of the SSTasim run. The mean RMSE with respect to all Glider observations decreases from 1.32 °C of the NoSSTasim run to 1.1 °C of the SSTasim run.

To further assess the model results, we categorize the relations between modeled and observed ocean surface temperature into four types (marked by different colors in Figure 8). Figure 9 shows the vertical temperature profile deviations which are classified according to the different types. Out of the 1507 improved temperature profiles, 1277 profiles (84.7%, blue in Figure 8a) are characterized by the situation that the simulated surface temperature of the NoSSTasim run is higher than the observed surface temperature of the Glider profile and that the simulated warm surface temperature bias decreases in the SSTasim run. The corresponding temperature profile deviations are shown as type IA in Figure 9. In this situation, the assimilation of the GMPE SST data reduces the simulated ocean surface temperature (Figure 9c) and consequently induces stronger vertical convection. Therefore, the information of lower surface temperatures can reach the deeper layers, and the simulated entire temperature profile improves (Figure 9d). However, if the modeled surface temperature of the NoSSTasim run is close to the Glider profile (Type DA in Figure 9a) and the modeled ocean surface cools in the SSTasim run (Type DA in Figure 9c) which leads to the amplification of surface temperature bias, the entire modeled temperature profile of the SSTasim run deteriorates (Type DA in Figure 9d) because too cold water (as imposed by the GMPE SST value) is convected by static instability. This happens for 291 in 481 deteriorated profiles (blue in Figure 8b).

Another situation (orange in Figure 8a and 8b) occurs when the modeled surface temperature of the NoSSTasim run is lower than the observed surface temperature of the Glider profile (Type IC and DC in Figure 9a) and the modeled surface temperature increases in the SSTasim run (Type IC and DC in Figure 9c). This warming leads to more stability and cannot penetrate to the deeper layers. This phenomenon is especially clear in the deteriorated profiles (Type DC in Figure 9d). For the other two types (green and red in Figure 8), the effects of SST assimilation depend on the individual vertical temperature gradients of the observations and the simulated profiles. For example, if the model surface temperature of the NoSSTasim run is lower than the observed surface temperature of the Glider profile (Type IB and DB in Figure 9a) and the modeled surface temperature decreases in the SSTasim run (Type IB and DB in Figure 9c), the simulated temperature profile improves in the case of the model subsurface temperature of the NoSSTasim run being higher than the observed subsurface temperature of the Glider profile (Type IB in Figure 9d), but it deteriorates in the case of the model subsurface temperature of the NoSSTasim run being lower than the observed subsurface temperature of the Glider profile (Type ID in Figure 9d).

We also compare model simulations with shipboard data. 1939 CTD profiles in the Norwegian Sea and the western Barents Sea, and 12786 records of ocean surface temperature were collected in 2012. Compared with the model simulations of the NoSSTasim run, 59% of the temperature profiles and 82% of the SST records are improved in the SSTasim run (not shown).

3.4 Comparison with MASIE-NH and AMSR data

The sea ice extent in 2012 is provided by the MASIE-NH data. The RMSE with respect to the MASIE-NH data decreases from 2.24 million km^2 in the CTRL run, to 2.15 million km^2 in the NoSSTasim run, and 2.12 million km^2 in the SSTasim run. Figure 10 shows the simulated and observed sea ice edge in March and September 2012. In September (Figure 10a), the CTRL run overestimates the sea ice extent (defined as where sea ice concentration is larger than 15%) compared to the observations. The sea ice data assimilation in the NoSSTasim run improves the simulated sea ice edge. In the SSTasim run, there is a slight further improvement of the sea ice edge simulation. In terms of the integrated ice edge error (IIEE; Goessling et al., 2016) computed with respect to the AMSR data for September, the error decreases from 2.41 million km^2 in the CTRL run, to 0.36 million km^2 in the NoSSTasim run, and 0.25 million km^2 in the SSTasim run. In March, the sea ice extent in the CTRL run is too small compared to observations. With data assimilation, the sea ice edge improves, especially in the Barents Sea, the Kara Sea and the Bering Sea (Figure 10b). The IIEE in March decreases from 1.95 million km^2 in the CTRL run, to 1.57 million km^2 in the NoSSTasim run, and 1.39 million km^2 in the SSTasim run.

In September, the ocean surface temperature in areas between the sea ice edge of the CTRL run and that of the NoSSTasim run is close to the freezing point, thus sea ice data assimilation can substantially improve the simulated sea ice edge (Figure 10a). In March, however, there are large sea ice edge deviations between the runs and observations in the Labrador Sea (Figure 10b) where the ocean surface in the NoSSTasim run is too warm (Figure 4). The ocean surface warm bias between the data assimilation runs and in situ observations are also quite large (not shown), thus sea ice created by the data assimilation melts immediately. The simulated sea ice edge in the Labrador Sea indicates that to accurately simulate the sea ice edge it is necessary to simulate the correct ocean surface temperature. Even with SST assimilation, this appears to be unsuccessful in the Labrador Sea in our simulations.

3.5 Comparison with BGEP ULS data

Besides the sea ice edge, the sea ice thickness is another critical variable for marine safety of commercial vessels. Figure 11 shows the time evolution of modeled and observed sea ice thickness in 2012 at three locations in the Beaufort Sea. From January to April, SMOS and Cryosat2 sea ice thickness observations are available. Thus the modeled sea ice thickness of both the NoSSTasim and SSTasim run are the result of the combination of the assimilated satellite sea ice thickness observations and sea ice thickness dynamics implemented in the numerical model. Between May and October, there are no sea ice thickness observations, so the simulated sea ice thickness evolution is determined by the model physics and the correlation between sea ice concentration, sea ice thickness and SST. The thickness assimilation in winter preconditions the sea ice appropriately, so that the summer sea ice thickness is also simulated more accurately. The long sea ice memory is attributed to the relatively slow melting and freezing processes (Day et al., 2014; Mu et al., 2018b).

Focusing on August to November, the sea ice data assimilation greatly reduces the sea ice extent where sea ice concentration is larger than 15% (Figure 10a). However, in the marginal sea ice zone in the Beaufort Sea where the sea ice concentration is below 15%, there are still patches of sea ice (Figure 11b, 11c). By assimilating SST data, these patches are removed when the ocean surface temperature is corrected (Figure 12).

4. Discussion and conclusion

In this paper, satellite-retrieved sea ice concentration, sea ice thickness and SST data are assimilated simultaneously into an Arctic sea ice-ocean model using a localized ensemble Kalman filter scheme. It is found that assimilating SST data in addition to sea ice concentration and sea ice thickness not only improves the upper ocean temperature simulation, but also improves the sea ice edge and sea ice extent simulations, as well as the sea ice thickness in the marginal sea ice zone. The effects of the SST data assimilation on upper ocean temperature improvements are not homogeneous. The improvements are significant in two situations: (1) when the simulated SST without data assimilation is warmer than the in situ observations, and when the assimilation reduces the SST warm bias. Hydrostatic instabilities favor the propagation of the cold surface signal induced by the SST assimilation downwards, and thus the entire upper ocean temperature simulation is improved. (2) When the simulated SST without data assimilation is colder than the in situ observations, and when the assimilation reduces the SST cold bias. In this situation, the improvements in the simulated ocean temperature due to the SST assimilation are restricted to the surface layers. The GMPE SST data used in this study is a median SST product from a multi-product ensemble. Stroh et al. (2015) suggested that state of the art SST products commonly have a cold temperature bias magnitude of less than -0.5 °C compared with in situ observations. The NoSSTasim run overestimates surface temperature in most areas of the North Atlantic Ocean and the Nordic Sea, the assimilation of the GMPE SST data corrects the model's warm surface bias. The thermal relationship between model surface temperature and assimilated SST data in the North Atlantic Ocean and the Nordic Sea contributes to the positive results in this study.

Assimilating sea ice concentration data can substantially improve the forecast of the sea ice edge location (Posey et al., 2015). Marginal sea ice is directly affected by horizontal heat advection of ocean surface currents. Thus the SST assimilation has the largest effects in the marginal sea ice zone (Figure 3d, 3f). Our results suggest that sea ice data assimilation only improves the sea ice edge simulation if ocean surface temperature is close to the freezing point. When the ocean surface temperature is unrealistically high, sea ice data assimilation cannot overcome this bias and consequently cannot simulate an accurate sea ice edge location (for example in the Labrador Sea in Figure 10b). During summer, assimilating sea ice data can correctly reduce the marginal sea ice zone, but when the surface water is too cold, continued freezing will form new ice. This process is suppressed by assimilating the correct SST data. As a consequence, SST data assimilation emerges as a key component in a sea ice forecasting system.

In the Labrador Sea, there is a large systematic SST bias in the simulation without data assimilation. SST data assimilation corrects the bias only in part. The covariance relationship, on which the data assimilation scheme is based, cannot entirely correct this systematic bias. In other words, the effect of SST data assimilation is small if the systematic SST bias is too large. The bias needs to be reduced prior to data assimilation, for example by tuning model parameters.

Because of the localization in the data assimilation algorithm and because the GMPE SST data are available only in ice free regions, the assessment of the upper ocean temperature and sea ice simulations is also mostly restricted to the ice free region or the vicinity of the sea ice edge. The sea ice data assimilation reduces sea ice extent and thickness. The freshwater volume increment of the surface layer leads to the decrease of the ocean surface salinity. Assimilating GMPE SST data diminishes the marginal sea ice in summertime, further reduces the ocean surface salinity (Figure 5b). Temperature and salinity observations under sea ice in the central Arctic Ocean are so scarce that we do not assess the temperature and salinity simulation in the pack ice areas in this study avoiding a necessarily unrepresentative evaluation of the upper ocean.

We have left aside the question of how the parameters of the data assimilation scheme affect the results. The parameters, such as the localized radius (Losa et al., 2012) and the uncertainties of the SSMIS sea ice concentration (Yang et al., 2014), will affect the solutions, but we anticipate that they will not lead to fundamentally different conclusions. Further the ensemble size has an influence on the results. While the chosen ensemble size of 23 members is sufficient for our application, larger ensembles will at least incrementally improve the results and should allow to use a larger localization radius, which can also contribute to improved results.

Our results suggest that for accurate sea ice edge forecasts, not only the ice state, but also the upper ocean state needs to be known. In this sense, further systematic improvements of sea ice forecasts to support the safety of marine operations in the Arctic may only be possible if ocean surface observations also under the ice cover become available. Closed loop simulations could elucidate the effect of under ice ocean temperature data to be able to understand whether such an effort is worth the high costs.

Acknowledgments. This work is supported by the National Key R&D Program of China (2017YFE0111700) and the Key Research Program of Frontier Sciences of Chinese Academy of Sciences (QYZDY-SSW-DQC021). This paper is a contribution to the Year of Polar Prediction (YOPP), a flagship activity of the Polar Prediction Project (PPP), initiated by the World Weather Research Programme (WWRP) of the World Meteorological Organization (WMO). The authors thank the University of Hamburg for providing the ASI-SSMI sea ice concentration data and SMOS sea ice thickness data, the University of Bremen for providing the AMSR sea ice edge data, the Alfred-Wegener-Institut, Helmholtz Zentrum für Polar- und Meeresforschung for providing the CryoSat-2 sea ice thickness data, the International Pacific Research Center for providing the Argo SDL data, the National Snow and Ice Data Center for providing the MASIE-NH data, the Woods Hole Oceanographic Institution for providing the BGEP ULS data, the European Centre for Medium-Range Weather Forecasts for providing the UKMO ensemble forecasting data, and the Copernicus Marine Environment Monitoring Service for providing the GMPE SST data, Glider data, CTD data, and SHIP OCCA data.

References and Citations

Anderson, J. L. (2001), An Ensemble Adjustment Kalman Filter for Data Assimilation, *Mon. Wea. Rev.,* 129, 2884-2903, doi:10.1175/1520-0493(2001)129.

Androsov, A., L. Nerger, R. Schnur, J. Schröter, A. Albertella, R. Rummel, R. Savcenko, W. Bosch, S. Skachko, and S. Danilov (2019), On the assimilation of absolute geodetic dynamic topography in a global ocean model: impact on the deep ocean state. *J. Geodesy.,* 93, 141-157, doi:10.1007/s00190-018-1151-1.

Bishop, C. H., B. J. Etherton, and S. J. Majumdar (2001), Adaptive sampling with the ensemble transform Kalman filter. Part I: Theoretical aspects. *Mon. Wea. Rev.,* 129, 420-436, doi:10.1175/1520-0493.

Bowler, N. E., A. Arribas, K. R. Mylne, K. B. Robertson, and S. E. Beare (2008), The MOGREPS short-range ensemble prediction system, *Q. J. R. Meteorol. Soc.,* 134: 703–722, https://doi.org/10.1002/qj.234.

Cavalieri, D. J., and C. L. Parkinson (2012), Arctic sea ice variability and trends, 1979-2010. *Cryosphere,* 6(4), 881-889, doi:10.5194/tc-6-881-2012.

Cavalieri, D. J., C. L. Parkinson, N. DiGirolamo, and A. Ivanoff (2012), Intersensor calibration between F13 SSMI and F17 SSMIS for global sea ice data records, IEEE Trans. *Geosci. Remote Sens.,* 9(2), 233-236.

Comiso, J. C., C. L. Parkinson, R. Gersten, and L. Stock (2008), Accelerated decline in the Arctic sea ice cover, *Geophys. Res. Lett.,* 35, L01703, doi:10.1029/2007GL031972.

Day, J. J., E. Hawkins, and S. Tietsche (2014), Will Arctic sea ice thickness initialization improve seasonal forecast skill?, *Geophys. Res. Lett.,* 41, 7566-7575, doi:10.1002/2014GL061694.

Evensen, G. (1994), Sequential data assimilation with a nonlinear quasi-geostrophic model using Monte Carlo methods to forecast error statistics. *J. Geophys. Res.,* 99, 10143–10162, doi:10.1029/94JC00572.

Fritzner, S., R. Graversen, K. H. Christensen, P. Rostosky, and K. Wang (2019), Impact of assimilating sea ice concentration, sea ice thickness and snow depth in a coupled ocean-sea ice modelling system, *Cryosphere,* 13, 491-509, doi:10.5194/tc-13-491-2019.

Gao, Y., J. Sun, F. Li, S. He, S. Sandven, Q. Yan, Z. Zhang, K. Lohmann, N. Keenlyside, T. Furevik, and L. Suo (2015), Arctic sea ice and Eurasian climate: A review, *Adv. Atmos. Sci.,* 32(1), 92-114.

Goessling, H. F., S. Tietsche, J. J. Day, E. Hawkins, and T. Jung (2016), Predictability of the Arctic sea ice edge, *Geophys. Res. Lett.,* 43, doi:10.1002/2015GL067232.

Jung, T., N. Gordon, P. Bauer, D. Bromwich, M. Chevallier, J. Day, J. Dawson, F. Doblas-Reyes, C. Fairall, H. Goessling, M. Holland, J. Inoue, T. Iversen, S. Klebe, P. Lemke, M. Losch, A. Makshtas, B. Mills, P. Nurmi, D. Perovich, P. Reid, I. Renfrew, G. Smith, G. Svensson, M. Tolstykh, and Q. Yang (2016), Advancing polar prediction capabilities on daily to seasonal time scales. *Bull. Amer. Meteor. Soc.,* doi:10.1175/BAMS-D-14-00246.1.

Kaleschke, L., C. Lupkes, T. Vihma, J. Haarpaintner, A. Bochert, J. Hartmann, and G. Heygster (2001), SSM/I sea ice remote sensing for mesoscale ocean-atmosphere interaction analysis. *Can. J. Remote Sens.,* 27, 526–537.

Kaleschke, L., N. Maaβ, C. Haas, S. Heygster, and R. Tonboe (2010), A sea-ice thickness retrieval model for 1.4 GHz radiometry and application to airborne measurements over low salinity sea-ice, *Cryosphere,* 4, 583-592, doi:10.5194/tc-4-583-2010.

Kaleschke, L., X. Tian-Kunze, N. Maaβ, M. Mäkynen, and M. Drusch (2012), Sea ice thickness retrieval from SMOS brightness temperatures during the Arctic freeze-up period, *Geophys. Res. Lett.,* 39, L05501, doi:10.1029/2012GL050916.

Laxon, S. W., K. A. Giles, A. L. Ridout, D. J. Wingham, R. Willatt, R. Cullen, R. Kwok, A. Schweiger, J. Zhang, C. Haas, S. Hendricks, R. Krishfield, N. Kurtz, S. Farrell and M. Davidson (2013), Cryosat-2 estimates of Arctic sea ice thickness and volume, *J. Geophys. Res.,* 40(4), 732-737, doi:10.1002/grl.50193.

Lellouche, J. M., O. Le Galloudec, M. Drévillon, C. Régnier, E. Greiner, G. Garric, N. Ferry, C. Desportes, C. E. Testut, C. Bricaud, R. Bourdallé-Badie, B. Tranchant, M. Benkiran, Y. Drillet, A. Daudin, and C. De Nicola (2013), Evaluation of global monitoring and forecasting systems at Mercator Océan, *Ocean Sci.,* 9, 57-81, doi:10.5194/os-9-57-2013.

Liang, X., Q. Yang, L. Nerger, S. N. Losa, B. Zhao, F. Zheng, L. Zhang, and L. Wu (2017), Assimilating Copernicus SST Data into a Pan-Arctic Ice-Ocean Coupled Model with a Local SEIK Filter, *J. Atmos. Ocean. Tech.,* 34(9), 1985-1999, doi:10.1175/JTECH-D-16-0166.1

Lisæter, K. A., G. Evensen, and S. Laxon (2007), Assimilating synthetic CryoSat sea ice thickness in a coupled ice-ocean model. *J. Geophys. Res.,* 112, C07023, doi:10.1029/2006JC003786.

Lisæter, K. A., J. Rosanova, and G. Evensen (2003), Assimilation of ice concentration in a coupled ice-ocean model, using the ensemble Kalman filter. *Ocean Dyn.,* 53, 368–388, doi:10.1007/s10236-003-0049-4.

Losa, S. N., S. Danilov, J. Schröter, L. Nerger, S. Maβmann, and F. Janssen (2012), Assimilating NOAA SST data into the BSH operational circulation model for the North and Baltic Seas: Inference about the data, *J. Mar. Syst.,* 105, 152-162.

Losch, M., D. Menemenlis, J. M. Campin, P. Heimbach, and C. Hill (2010), On the formulation of sea-ice models. Part 1: Effects of different solver implementations and parameterizations. Ocean Model., 33, 129–144.

Madsen, K. S., T. A. S. Rasmussen, M. H. Ribergaard, and I. M. Ringgaard (2015), High resolution sea ice modelling and validation of the Arctic with focus on south Greenland waters, 2004-2013. *Polarforschung,* 85(2), 101-105, doi:10.2312/polfor.2016.006.

Marshall, J., A. Adcroft, C. Hill, L. Perelman, and C. Heisey (1997), A finite-volume, incompressible Navier Stokes model for studies of the ocean on parallel computers, *J. Geophys. Res.,* 102(C3), 5753-5766, doi:10.1029/96JC02775.

Melling, H., P. Johnston, and D. Riedel (1995), Measurements of the underside topography of sea ice by moored subsea sonar, *J. Atmos. Ocean. Tech.,* 12(3), 589-602.

Menemenlis, D., J. M. Campin, P. Heimbach, C. Hill, T. Lee, A. Nguyen, M. Schodlok, and H. Zhang (2008), ECCO2: High resolution global ocean and sea ice data synthesis, *Mercator Ocean Q. Newsl.,* 31, 13–21.

Mu, L., Q. Yang, M. Losch, S. N. Losa, R. Ricker, L. Nerger, and X. Liang (2018a), Improving sea ice thickness estimates by assimilating cryosat-2 and smos sea ice thickness data simultaneously, *Q. J. R. Meteorol. Soc.,* 144(711), 529-538.

Mu, L., M. Losch, Q. Yang, R. Ricker, S. Losa, and L. Nerger (2018b), Arctic-wide sea-ice thickness estimates from combining satellite remote sensing data and a dynamic ice-ocean model with data assimilation during the CryoSat-2, *J. Geophys. Res. Oceans,* doi:10.1029/2018JC014316.

National Ice Center and National Snow and Ice Data Center. Compiled by F. Fetterer, M. Savoie, S. Helfrich, and P. Clemente-Colón. 2010, updated daily. Multisensor

Analyzed Sea Ice Extent - Northern Hemisphere (MASIE-NH), Version 1. [January to December 2012]. Boulder, Colorado USA. NSIDC: National Snow and Ice Data Center. doi: https://doi.org/10.7265/N5GT5K3K. Accessed November 27, 2017.

Nerger, L., S. Danilov, W. Hiller, and. J. Schröter (2006). Using sea-level data to constrain a finite-element primitive-equation ocean model with a local SEIK filter, *Ocean Dyn.,* 56, 634-649, doi: 10.1007/s10236-006-0083-0.

Nerger, L., and W. Hiller (2013), Software for ensemble-based data assimilation systems-implementation strategies and scalability, *Comput. Geosci.,* 55, 110-118, doi:10.1016/j.cageo.2012.03.026.

Nerger, L., T. Janji, J. Schröter, and W. Hiller (2012a), A unification of ensemble square root Kalman filters, *Mon. Weather. Rev.,* 140(7), 2335-2345.

Nguyen, A. T., D. Menemenlis, and R. Kwok (2011), Arctic ice-ocean simulation with optimized model parameters: Approach and assessment, *J. Geophys. Res.,* 116(C4), doi:10.1029/2010JC006573.

Pham, D. T. (2001), Stochastic methods for sequential data assimilation in strongly nonlinear systems. *Mon. Wea. Rev.,* 129, 1194–1207, doi:10.1175/1520-0493.

Posey, P. G., E. J. Metzger, A. J. Wallcraft, R. H. Preller, O. M. Smedstad, and M. W. Phelps (2010), Validation of the 1/12° Arctic Cap Nowcast/Forecast System (ACNFS), NRL report NRL/MR/7320-10-9287, Stennis Space Center, MS.

Posey, P. G., E. J. Metzger, A. J. Wallcraft, D. A. Hebert, R. A. Allard, O. M. Smedstad, M. W. Phelps, F. Fetterer, J. S. Stewart, W. N. Meier, and S. R. Helfrich (2015), Improving Arctic sea ice edge forecasts by assimilating high horizontal resolution sea ice concentration data into the US Navy's ice forecast systems, *Cryosphere*, 9(4), 1735–1745.

Proshutinsky, A., J. Yang, R. Krishfield, R. Gerdes, M. Karcher, F. Kauker, C. Koeberle, S. Hakkinen, W. Hibler, D. Holland, M. Maqueda, G. Holloway, E. Hunke, W. Maslowski, M. Steele, and J. Zhang (2005), Arctic Ocean Study: Synthesis of Model Results and Observations, *EOS*, 86 (40), 368-371.

Ricker, R., S. Hendricks, V. Helm, H. Skourup, and M. Davidson (2014), Sensitivity of CryoSat-2 Arctic sea ice freeboard and thickness on radar-waveform interpretation, *Cryosphere,* 8(4), 1607-1622, doi:10.5194/tc-8-1607-2014.

Rojas-Romagosa, H., E. Bekkers, and J. F. Francois (2016), Melting Ice Caps and the Economic Impact of Opening the Northern Sea Route. *Economic Journal,* 128(1).

Sakov, P., F. Counillon, L. Bertino, K. A. Lisæter, P. R. Oke, and A. Korablev (2012), TOPAZ4: An ocean-sea ice data assimilation system for the North Atlantic and Arctic. *Ocean Sci.,* 8, 633–656, doi:10.5194/os-8-633-2012.

Smith, G. C., F. Roy, M. Reszka, D. S. Colan, Z. He, D. Deacu, J. M. Belanger, S. Skachko, Y. Liu, F. Dupont, J. F. Lemieux, C. Beaudoin, B. Tranchant, M. Drevillon, G. Garric, C. E. Testut, J. M. Lellouche, P. Pellerin, H. Ritchie, Y. Lu, F. Davidson, M. Buehner, A. Caya and M. Lajoie (2016), Sea ice forecast verification in the Canadian Global Ice Ocean Prediction System. *Q. J. R. Meteorol. Soc.,* 142(695): 659-671.

Spreen, G., L. Kaleschke, and G.Heygster (2008), Sea ice remote sensing using AMSR-E 89 GHz channels, *J. Geophys. Res.,* vol. 113, C02S03, doi:10.1029/2005JC003384.

Stroh, J. N., G. Panteleev, S. Kirillov, M. Makhotin, and N. Shakhova (2015), Sea-surface temperature and salinity product comparison against external in situ data in the Arctic Ocean, *J. Geophys. Res. Oceans.,* 120, 7223-7236, doi:10.1002/2015JC011005.

Tian-Kunze, X., L. Kaleschke, N. Maaβ, M. Mäkynen, N. Serra, M. Drusch, and T. Krumpen (2014), SMOS-derived thin sea ice thickness: Algorithm baseline, product specifications and initial verification, *Cryosphere,* 8, 997-1018, doi:10.5194/tc-8-997-2014.

Wingham, D. J., C. R. Francis, S. Baker, C. Bouzinac, D. Brockley, R. Cullen, P. de Chateau-Thierry, S. W. Laxon, U. Mallow, C. Mavrocordatos, L. Phalippou, G. Ratier, L. Rey, F. Rostan, P. Viau, and D. W. Wallis (2006), Cryosat: A mission to determine the fluctuations in Earths land and marine ice fields, *Adv. Sp. Res.,* 37(4), 841-871, doi:10.1016/j.asr.2005.07.027.

Yang, Q., S. N. Losa, M. Losch, X. Tian-Kunze, L. Nerger, J. Liu, L. Kaleschke, and Z. Zhang (2014), Assimilating SMOS sea ice thickness into a coupled ice-ocean model using a local SEIK filter. *J. Geophys. Res. Oceans,* 119, 6680–6692, doi:10.1002/2014JC009963.

Yang, Q., S. N. Losa, M. Losch, T. Jung, and L. Nerger (2015a), The role of atmospheric uncertainty in Arctic summer sea ice data assimilation and prediction. *Q. J. R. Meteorol. Soc.,* 141, 2314–2323, doi:10.1002/qj.2523.

Yang, Q., S. N. Losa, M. Losch, J. Liu, Z. Zhang, L. Nerger, and H. Yang (2015b), Assimilating summer sea-ice concentration into a coupled ice-ocean model using a LSEIK filter, *Ann. Glaciol.,* 56 (69), 38-44.

Yang, Q., M. Losch, S. N. Losa, T. Jung, L. Nerger, and T. Lavergne (2016), Brief communication: The challenge and benefit of using sea ice concentration satellite data products with uncertainty estimates in summer sea ice data assimilation, *Cryosphere,* 10 (2), 761-774, doi:10.5194/tc-10-761-2016.

Zhang, J., and W. D. Hibler (1997), III, On an efficient numerical method for modeling sea ice dynamics, *J. Geophys. Res.,* 102(C4), 8691-8702, doi:10.1029/96JC03744.

Zhang, Y. -F., C. M. Bitz, J. L. Anderson, N. Collins, J. Hendricks, T. Hoar, K. Raeder and F. Massonnet (2018), Insights on Sea Ice Data Assimilation from Perfect Model Observing System Simulation Experiments, *J. Climate,* 31, 5911-5926, doi:10.1175/JCLI-D-17-0904.1

Figure Captions

Figure 1. (a) Number of days with available potential temperature observations and (b) mean uncertainties of the observations (°C) in 2012 in GMPE data. Values in the Gulf of Alaska and the Okhotsk Sea are set to zero.

Figure 2. Setup of experiments: CTRL without data assimilation; NoSSTasim assimilating only sea ice data; SSTasim assimilating sea ice and SST data.

Figure 3. Spatial distributions of the RMSD of SST in °C (upper row), sea ice concentration (middle row), sea ice thickness in m (lower row) between the NoSSTasim and CTRL runs (left column), between the SSTasim and NoSSTasim runs (right column).

Figure 4. Spatial distribution of the annual mean SST bias in °C between the NoSSTasim run and the GMPE SST data. The values are averaged in 2012 when the GMPE data are available.

Figure 5. Vertical distribution of (a) mean ocean temperature in °C south of 75 °N, (b) mean ocean salinity north of 75 °N for the SSTasim (red), NoSSTasim (blue), and CTRL (black) runs.

Figure 6. Vertical distribution of (a) the RMSE and (b) mean bias of ocean temperature in °C with respect to the Argo SDL data for the SSTasim (red dots), NoSSTasim (blue dots), and CTRL (black crosses) runs, (c) number of the Argo SDL observations at each standard depth level.

Figure 7. Spatial distribution of the RMSE of ocean temperature in °C with respect to the Argo SDL data at 200 m depth for (a) the NoSSTasim, and (b) SSTasim runs.

Figure 8. Locations of the Glider profiles in 2012 where the RMSE of the entire temperature profile between the SSTasim run and the observed profile is (a) smaller or (b) larger than that between the NoSSTasim run and the observed profile. The colors denote the Glider locations where the surface temperature of the NoSSTasim run is (blue) higher than that of the Glider profile and also higher than that of the

SSTasim run, (green) lower than that of the Glider profile but higher than that of the SSTasim run, (orange) lower than that of the Glider profile and also lower than that of the SSTasim run, (red) higher than that of the Glider profile but lower than that of the SSTasim run.

Figure 9. Vertical distributions of temperature deviations in °C (a) between the NoSSTasim run and Glider profiles, (b) between the SSTasim run and Glider profiles, (c) between the SSTasim and NoSSTasim run, (d) between the absolute value of (a) and absolute value of (b). The labels IA to ID and DA to DD present the profile types shown in Figure 8a: IA-blue, IB-green, IC-orange, ID-red and Figure 8b: DA-blue, DB-green, DC-orange, DD-red.

Figure 10. Sea ice edge in (a) September and (b) March in 2012. The purple patch denotes the area where the sea ice concentration from AMSR is larger than 15%. The lines denote the sea ice edge in the CTRL run (blue), in the NoSSTasim run (green), and in the SSTasim run (red).

Figure 11. Time evolution of sea ice thickness in meters at three positions: (a) 75 °N, 150 °W, (b) 78 °N, 150 °W, (c) 74 °N, 140 °W. The blue, green, red lines denote sea ice thickness of the CTRL run, the NoSSTasim run, the SSTasim run, respectively. The black solid and dashed lines denote sea ice thickness observations of BGEP ULSs which were deployed in the summers of 2011 and 2012. The black lines of BGEP ULS observations have been smoothed with the gray bar representing the observational uncertainty. The cyan and pink crosses denote the assimilated CryoSat-2 and SMOS sea ice thickness observations, respectively.

Figure 12. September sea ice concentration in 2012 in marginal sea ice zone of (a) the NoSSTasim run, and (b) the SSTasim run. White areas represent concentrations above 15% and ice free regions.

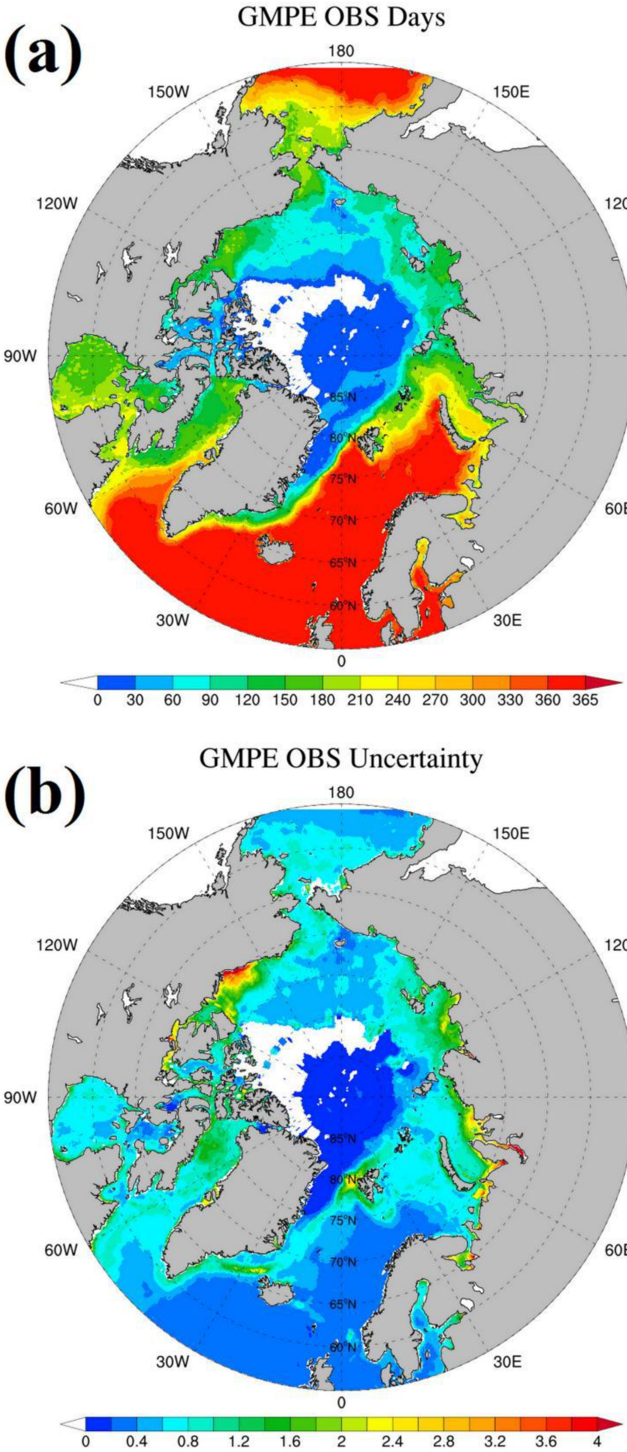

Figure 1. (a) Number of days with available potential temperature observations and (b) mean uncertainties of the observations (°C) in 2012 in GMPE data. Values in the Gulf of Alaska and the Okhotsk Sea are set to zero.

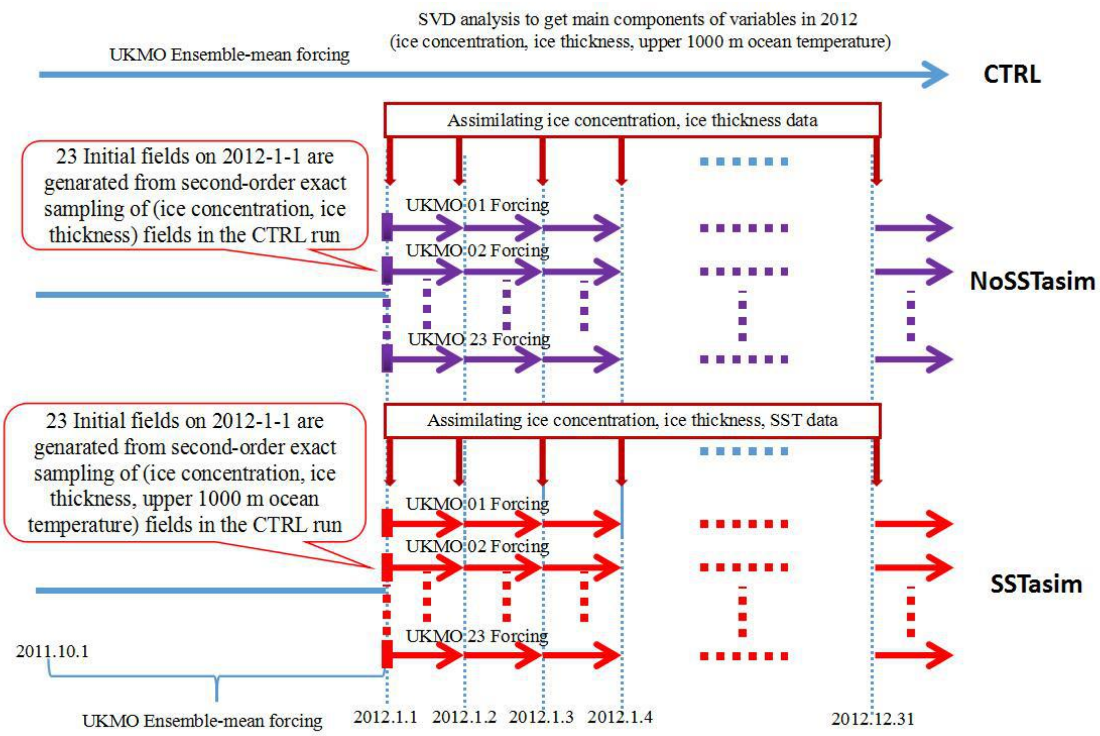

Figure 2. Setup of experiments: CTRL without data assimilation; NoSSTasim assimilating only sea ice data; SSTasim assimilating sea ice and SST data.

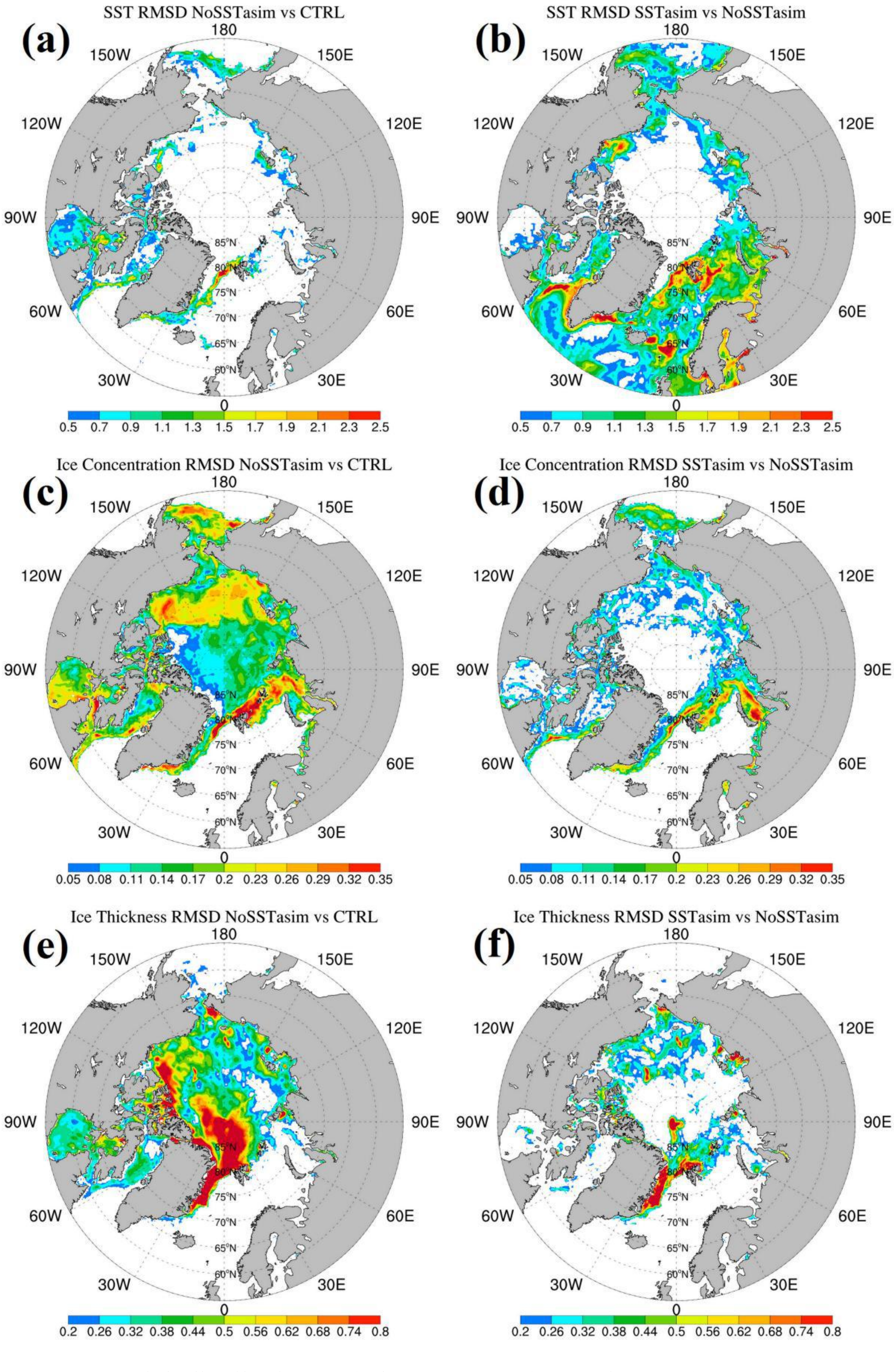

Figure 3. Spatial distributions of the RMSD of SST in °C (upper row), sea ice concentration (middle row), sea ice thickness in m (lower row) between the NoSSTasim and CTRL runs (left column), between the SSTasim and NoSSTasim runs (right column).

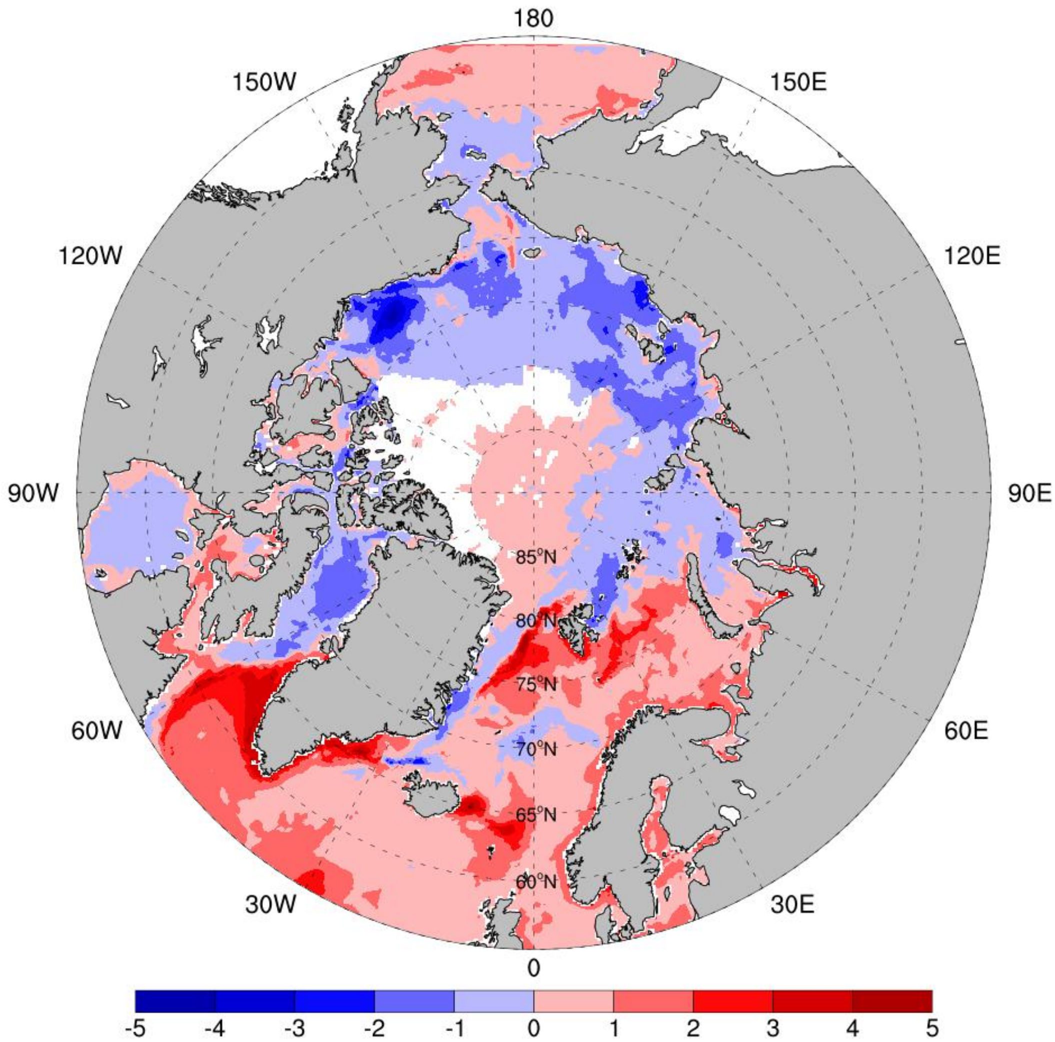

Figure 4. Spatial distribution of the annual mean SST bias in °C between the NoSSTasim run and the GMPE SST data. The values are averaged in 2012 when the GMPE data are available.

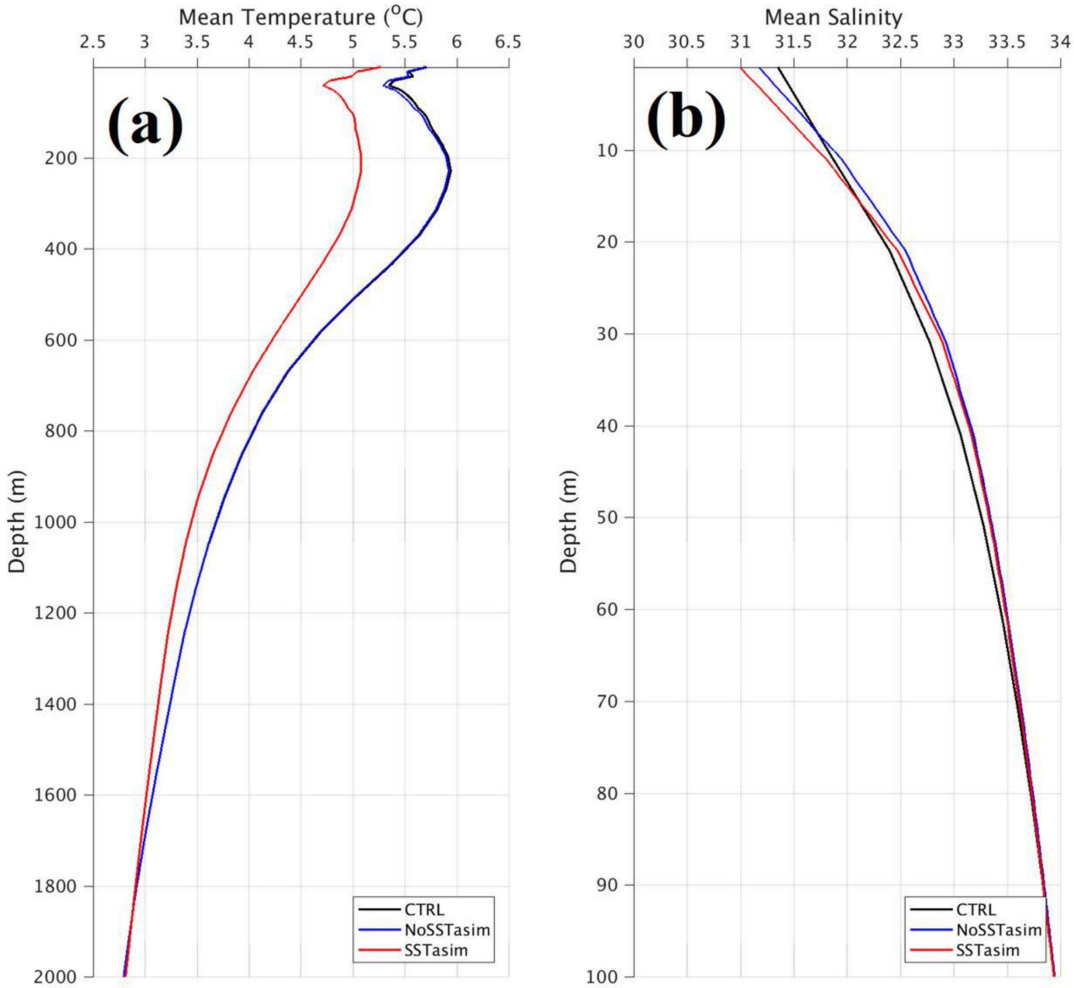

Figure 5. Vertical distribution of (a) mean ocean temperature in °C south of 75 °N, (b) mean ocean salinity north of 75 °N for the SSTasim (red), NoSSTasim (blue), and CTRL (black) runs.

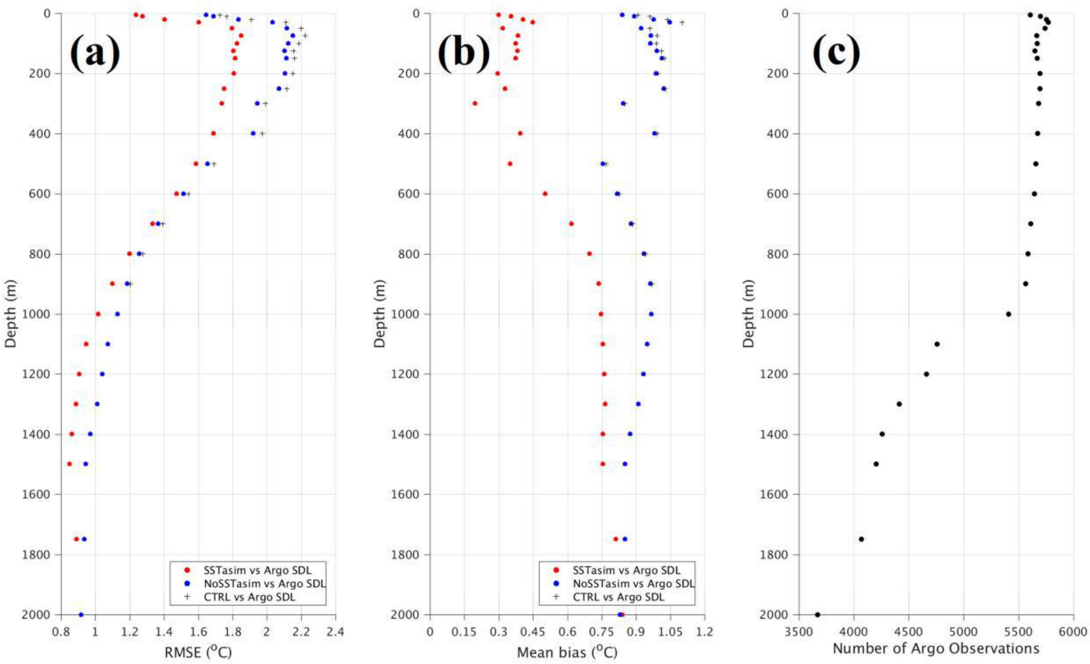

Figure 6. Vertical distribution of (a) the RMSE and (b) mean bias of ocean temperature in °C with respect to the Argo SDL data for the SSTasim (red dots), NoSSTasim (blue dots), and CTRL (black crosses) runs, (c) number of the Argo SDL observations at each standard depth level.

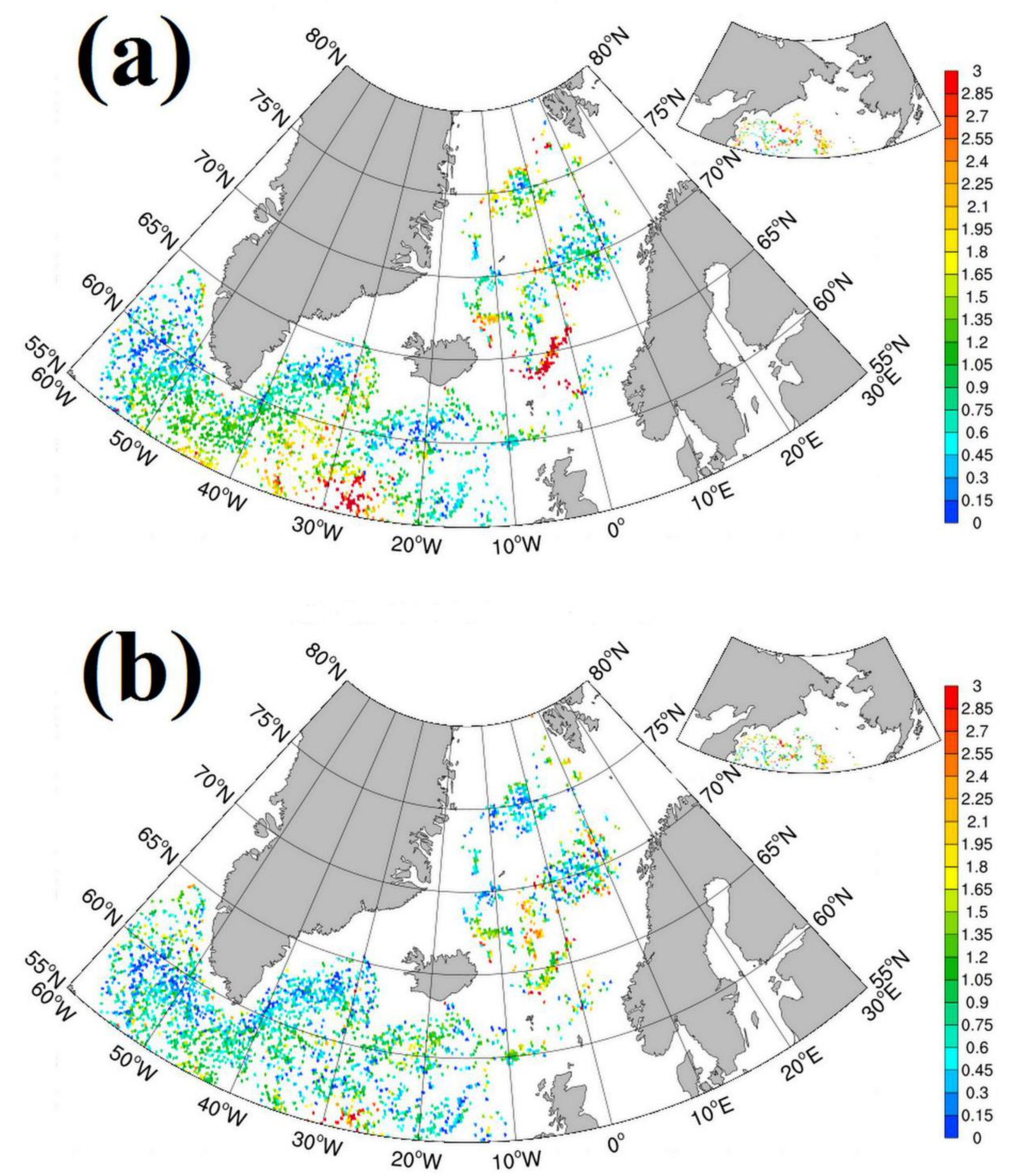

Figure 7. Spatial distribution of the RMSE of ocean temperature in °C with respect to the Argo SDL data at 200 m depth for (a) the NoSSTasim, and (b) SSTasim runs.

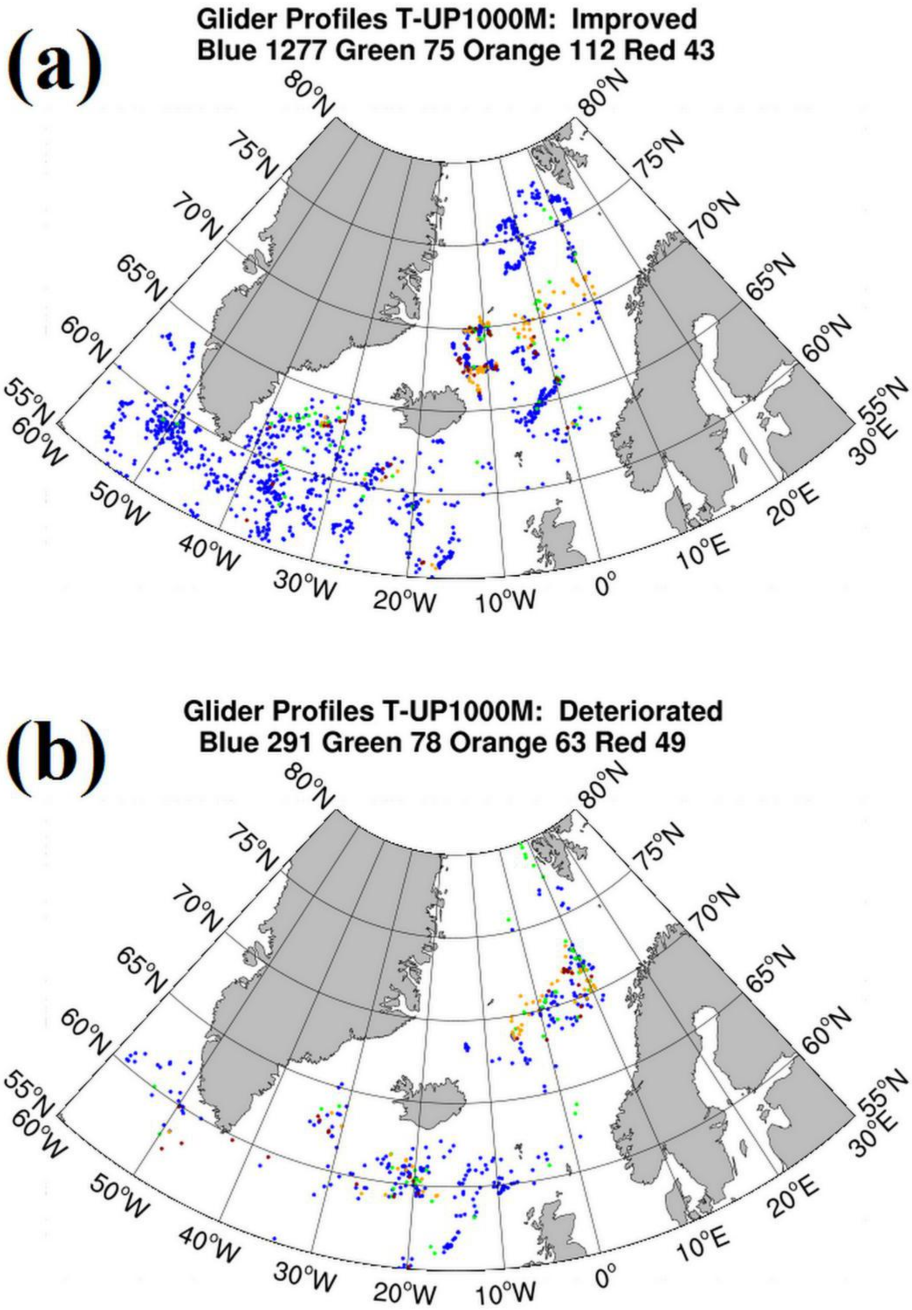

Figure 8. Locations of the Glider profiles in 2012 where the RMSE of the entire temperature profile between the SSTasim run and the observed profile is (a) smaller or (b) larger than that between the NoSSTasim run and the observed profile. The colors denote the Glider locations where the surface temperature of the NoSSTasim run is (blue) higher than that of the Glider profile and also higher than that of the SSTasim run, (green) lower than that of the Glider profile but higher than that of the SSTasim run, (orange) lower than that of the Glider profile and also lower than that of the SSTasim run, (red) higher than that of the Glider profile but lower than that of the SSTasim run.

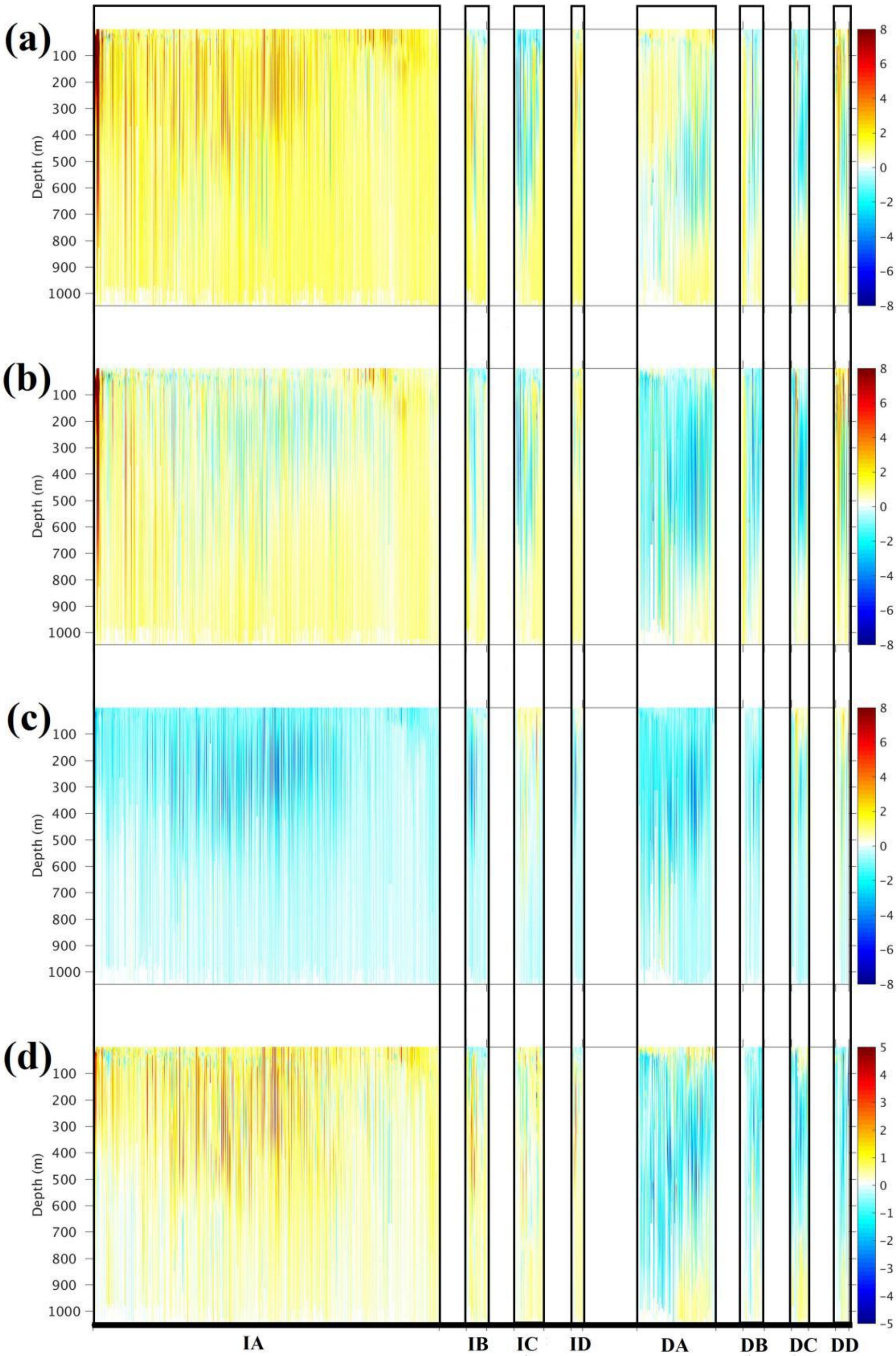

Figure 9. Vertical distributions of temperature deviations in °C (a) between the NoSSTasim run and Glider profiles, (b) between the SSTasim run and Glider profiles, (c) between the SSTasim and NoSSTasim run, (d) between the absolute value of (a) and absolute value of (b). The labels IA to ID and DA to DD present the profile types shown in Figure 8a: IA-blue, IB-green, IC-orange, ID-red and Figure 8b: DA-blue, DB-green, DC-orange, DD-red.

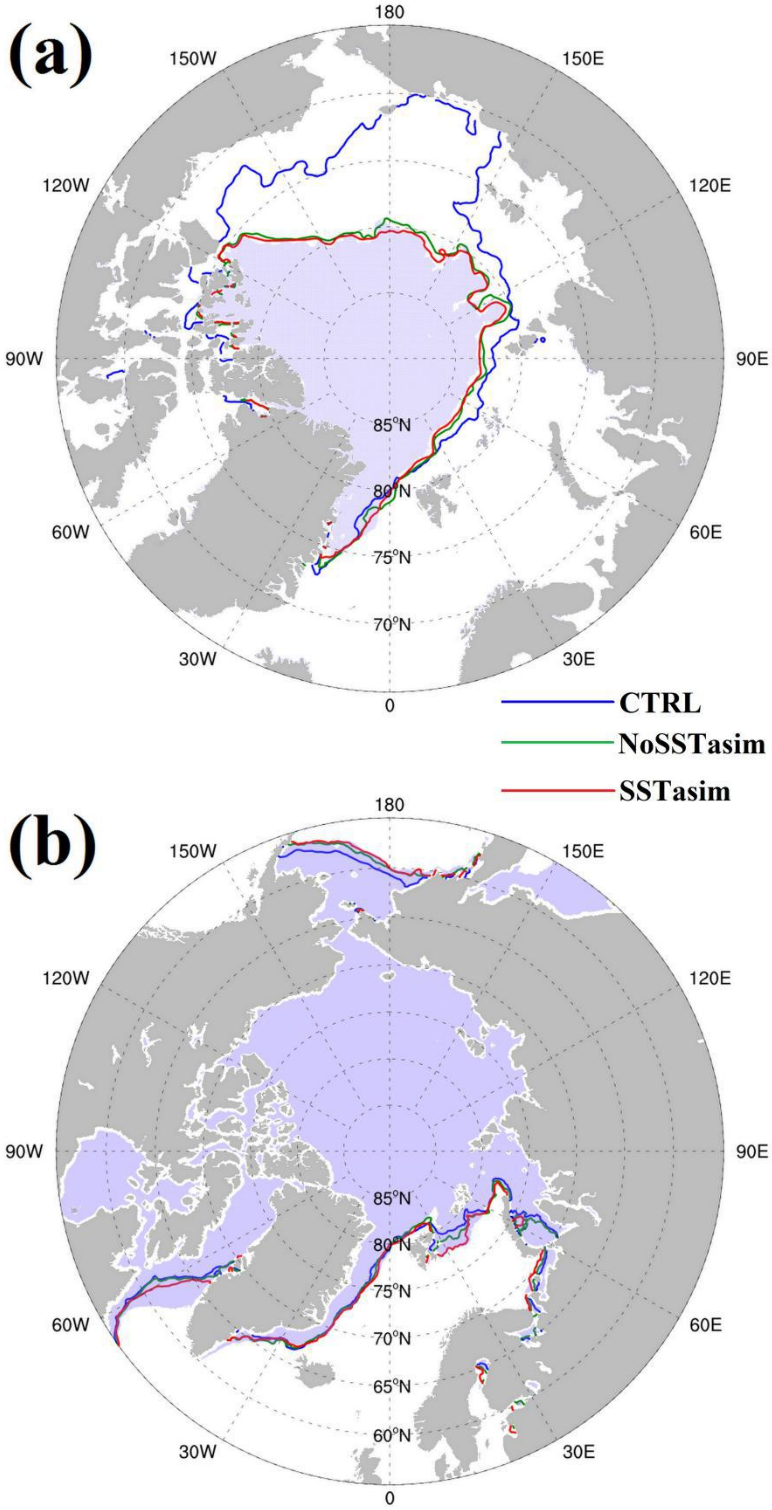

Figure 10. Sea ice edge in (a) September and (b) March in 2012. The purple patch denotes the area where the sea ice concentration from AMSR is larger than 15%. The lines denote the sea ice edge in the CTRL run (blue), in the NoSSTasim run (green), and in the SSTasim run (red).

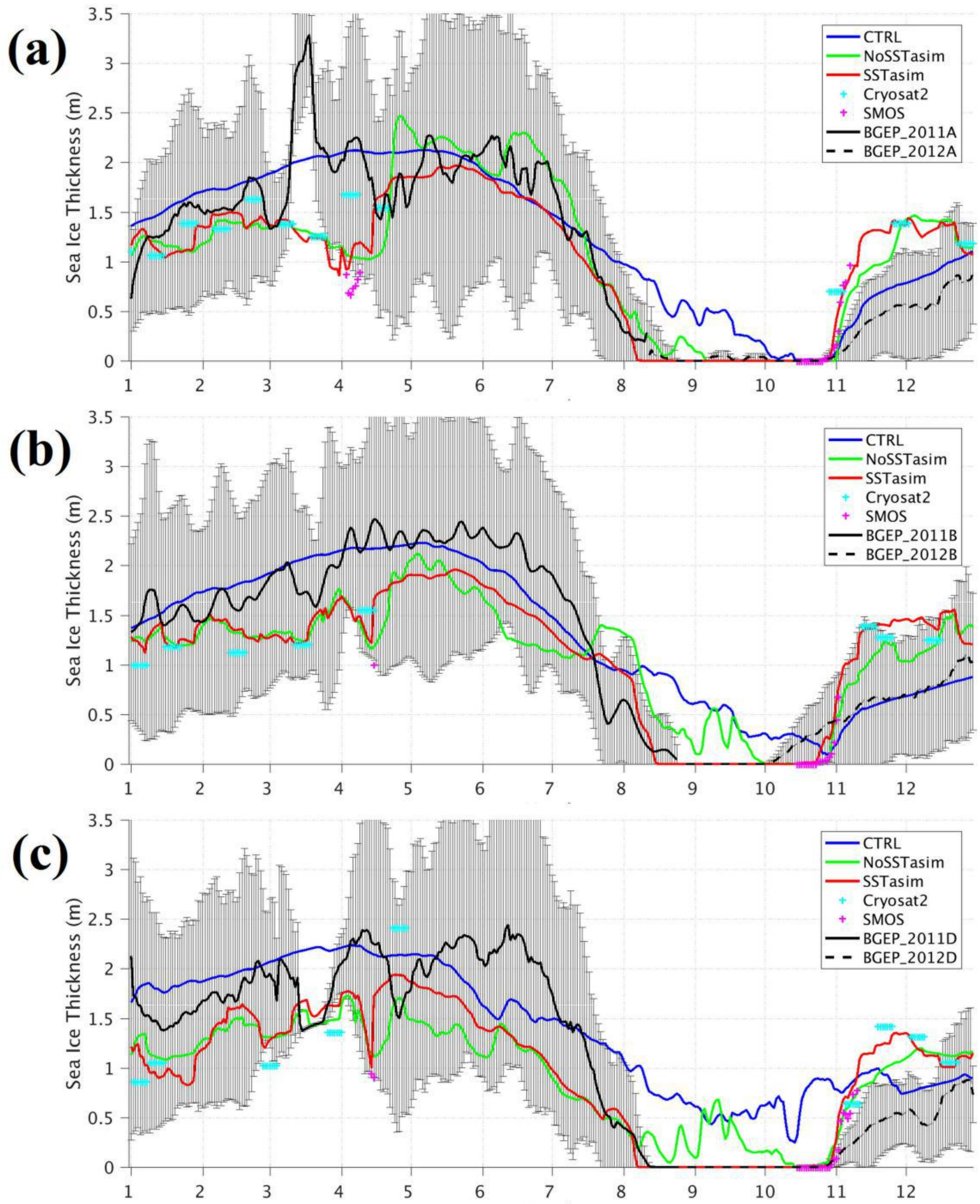

Figure 11. Time evolution of sea ice thickness in meters at three positions: (a) 75 °N, 150 °W, (b) 78 °N, 150 °W, (c) 74 °N, 140 °W. The blue, green, red lines denote sea ice thickness of the CTRL run, the NoSSTasim run, the SSTasim run, respectively. The black solid and dashed lines denote sea ice thickness observations of BGEP ULSs which were deployed in the summers of 2011 and 2012. The black lines of BGEP ULS observations have been smoothed with the gray bar representing the observational uncertainty. The cyan and pink crosses denote the assimilated CryoSat-2 and SMOS sea ice thickness observations, respectively.

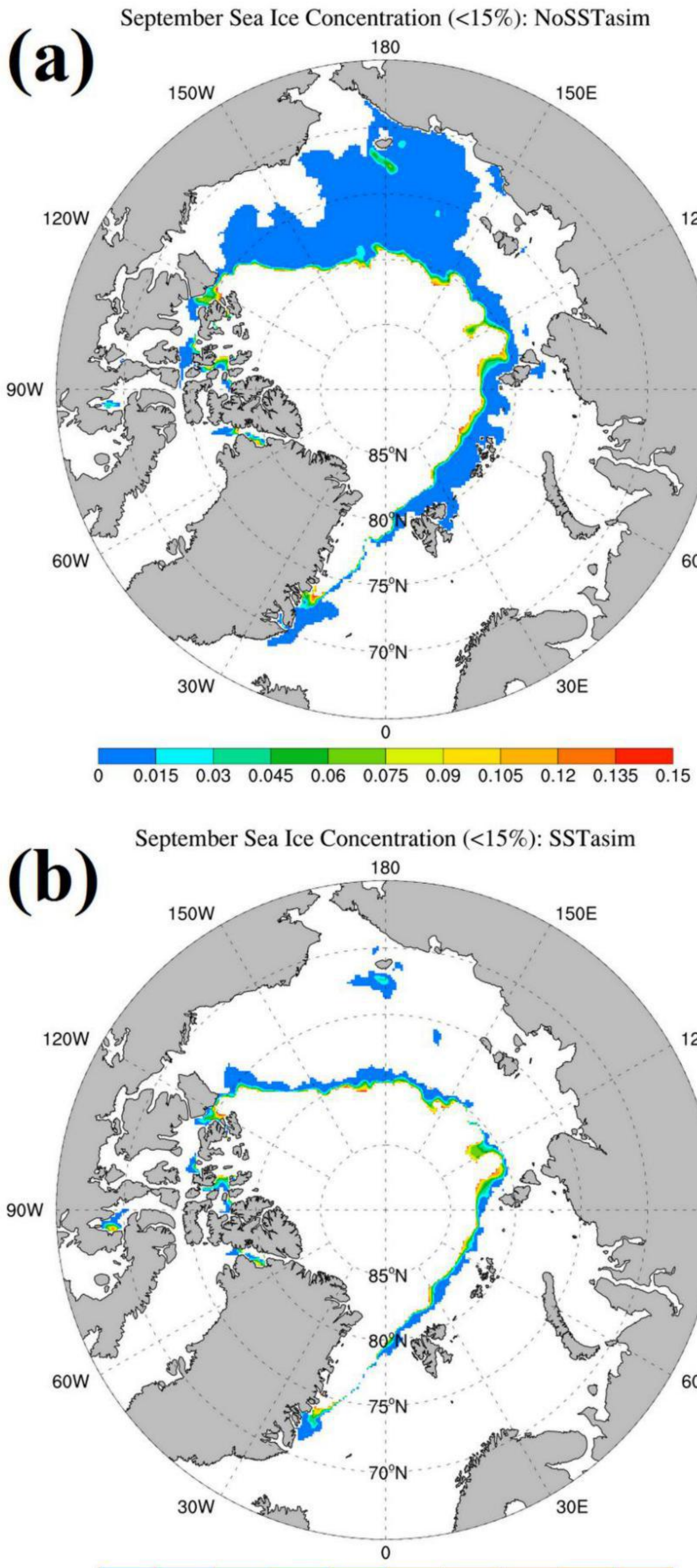

Figure 12. September sea ice concentration in 2012 in marginal sea ice zone of (a) the NoSSTasim run, and (b) the SSTasim run. White areas represent concentrations above 15% and ice free regions.

Table 1. Regional mean RMSE of ocean temperature in °C with respect to the Argo SDL data. The high latitude western Atlantic Ocean (HLWAO) refers to the area enclosed by the longitudes 45°W to 70°W and the latitudes 55°N to 65°N. The high latitude central Atlantic Ocean (HLCAO) refers to the area enclosed by the longitudes 20°W to 45°W and the latitudes 55°N to 65°N. The high latitude eastern Atlantic Ocean (HLEAO) refers to the area enclosed by the longitudes 20°W to 15°E and the latitudes 55°N to 65°N.

		HLWAO	HLCAO	HLEAO	Greenland Sea	Bering Sea
10 m	NoSSTasim	1.84	1.11	0.89	0.85	0.91
	SSTasim	1.28	0.71	0.37	0.41	0.67
200 m	NoSSTasim	1.25	1.87	1.22	1.21	1.76
	SSTasim	1.13	1.49	0.94	1.01	1.54
1500 m	NoSSTasim	0.72	1.03	1.13	0.80	0.12
	SSTasim	0.60	0.96	1.00	0.68	0.21